Article

Active Site Structure of Class I Ribonucleotide Reductase Intermediate X: A Density Functional Theory Analysis of Structure, Energetics, and Spectroscopy

Wen-Ge Han, Tiqing Liu, Timothy Lovell, and Louis Noodleman

J. Am. Chem. Soc., **2005**, 127 (45), 15778-15790• DOI: 10.1021/ja050904q • Publication Date (Web): 19 October 2005

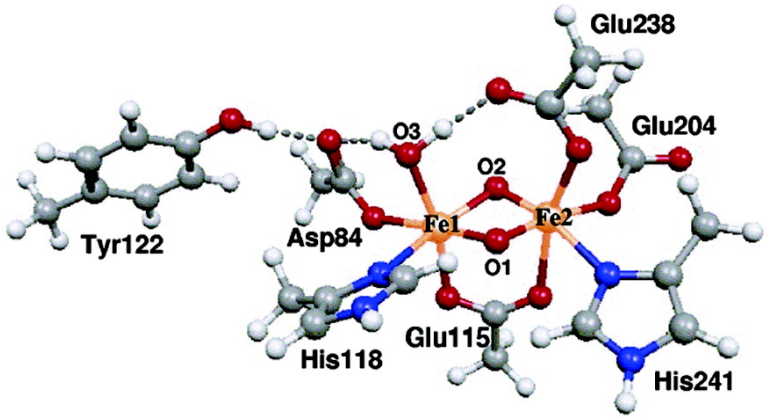

More About This Article

Additional resources and features associated with this article are available within the HTML version:

- Supporting Information
- Links to the 8 articles that cite this article, as of the time of this article download
- Access to high resolution figures
- Links to articles and content related to this article
- Copyright permission to reproduce figures and/or text from this article

View the Full Text HTML

J|A|C|S
ARTICLES
Published on Web 10/19/2005

Active Site Structure of Class I Ribonucleotide Reductase Intermediate X: A Density Functional Theory Analysis of Structure, Energetics, and Spectroscopy

Wen-Ge Han,* Tiqing Liu,† Timothy Lovell,‡ and Louis Noodleman*

Contribution from the Department of Molecular Biology, TPC15, The Scripps Research Institute, 10550 North Torrey Pines Road, La Jolla, California 92037

Received February 11, 2005; E-mail: wengehan@scripps.edu; lou@scripps.edu

Abstract: Several models for the active site structure of class I ribonucleotide reductase (RNR) intermediate X have been studied in the work described in this paper, using broken-symmetry density functional theory (DFT) incorporated with the conductor-like screening (COSMO) solvation model. The calculated properties, including geometries, spin states, ^{57}Fe, ^{1}H, and ^{17}O hyperfine tensors, Mössbauer isomer shifts, and quadrupole splittings, and the estimation of the Fe(IV) d−d transition energies have been compared with the available experimental values. On the basis of the detailed analysis and comparisons, we propose a definite form for the active site structure of class I RNR intermediate X, which contains an Fe1(III)Fe2(IV) center (where Fe1 is the iron site closer to Tyr122, and the two iron sites are high-spin antiferromagnetically coupled to give a total $^{1}/_{2}$ net spin), two μ-oxo bridges, one terminal water which binds to Fe1(III) and also H-bonds to both side chains of Asp84 and Glu238, and one bidentate carboxylate group from the side chain of Glu115.

1. Introduction

Ribonucleotide reductase (RNR) catalyzes the reduction of ribonucleotides (NTPs) to their 2′-deoxyribonucleotide (dNTP) counterparts, which are the precursors required in the initial step of DNA biosynthesis.[1,2] The well-characterized RNR forms can be grouped into three classes. Though different RNR classes differ in composition and cofactor requirements, they display a reaction mechanism with a common theme using metals and free radical chemistry. In the present work, attention is exclusively restricted to class I RNR, which has been found in all eukaryotes, some prokaryotes, and several viruses.[3]

The class I RNRs consist of a homodimer of two dissimilar protein subunits, R1 and R2, in an overall $\alpha_2\beta_2$ tetramer. Subunit R1 contains the substrate (NTP) binding site and catalyzes the dehydroxylation of the 2′-hydroxyl group of the ribose ring. Subunit R2 contains one binuclear iron cluster, which generates and stabilizes a radical at a tyrosine (Tyr122 in *Escherichia coli*; all residue notations in this paper reflect those from *E. coli*) which is close to the diiron center. This radical functions as a "pilot light" which begins the catalytic reaction by a long-range proton-coupled electron-transfer process to generate a thiyl radical on cysteine 439 of subunit R1, which then performs the nucleotide reduction.[4] Though some exceptions have been found for the mouse and Chlamydiae,[5a,b] this radical-bearing tyrosine is conserved among more than 200 sequenced R2s, and mutants with a phenylalanine in this position are enzymatically inactive.[5c,d] This tyrosine radical has been identified in the oxidized deprotonated form and is stable for days at room temperature.[1] Once this radical is lost, the enzyme becomes inactive, but the active form can be regenerated by two-electron reduction of the diferric met form from a reductase protein followed by O_2 binding. The overall net reaction cycle is given by

$$\mathrm{Fe(III)}(\mu\text{-O})(\mathrm{OH}_n)\mathrm{Fe(III)}-\mathrm{Tyr122}-\mathrm{OH} + 2\mathrm{e}^- + (4-n)\mathrm{H}^+ \rightarrow \mathrm{Fe(II)Fe(II)}-\mathrm{Tyr122}-\mathrm{OH} + 2\mathrm{H_2O} \quad \text{(I)}$$

$$\mathrm{Fe(II)Fe(II)}-\mathrm{Tyr122}-\mathrm{OH} + \mathrm{O_2} + \mathrm{e}^- + n\mathrm{H}^+ \rightarrow \mathrm{Fe(III)}(\mu\text{-O})(\mathrm{OH}_n)\mathrm{Fe(IV)}-\mathrm{Tyr122}-\mathrm{OH} \quad \text{(II)}$$

$$\mathrm{Fe(III)}(\mu\text{-O})(\mathrm{OH}_n)\mathrm{Fe(IV)}-\mathrm{Tyr122}-\mathrm{OH} \rightarrow \mathrm{Fe(III)}(\mu\text{-O})(\mathrm{OH}_n)\mathrm{Fe(III)}-\mathrm{Tyr122}-\mathrm{O}^{\bullet} + \mathrm{H}^+ \quad \text{(III)}$$

where $n = 0$, 1, or 2. This reaction occurs in a complicated sequence of steps with structure rearrangement and with coupled electron and proton transfers. If $n = 0$ in eq II, the resulting intermediate is Fe(III)Fe(IV) di-μ-oxo. The "free" proton extracted from Tyr122 then likely protonates the cluster oxygen

† Present address: University of Maryland Biotechnology Institute, Center for Advanced Research in Biotechnology, 9600 Gudelsky Dr., Rockville, MD 20850.

‡ Present address: AstraZeneca R and D Molndal, SE-431 83, Molndal, Sweden.

(1) Wallar, B. J.; Lipscomb, J. D. *Chem. Rev.* **1996**, *96*, 2625−2657.
(2) Sjöberg, B. M. *Struct. Bonding* **1997**, *88*, 139−173.
(3) Fontecave, M.; Nordlund, P.; Eklund, H.; Reichard, P. *Adv. Enzymol. Relat. Areas Mol. Biol.* **1992**, *65*, 147−183.
(4) (a) Sturgeon, B. E.; Burdi, D.; Chen, S.; Huynh, B. H.; Edmondson, D. E.; Stubbe, J.; Hoffman, B. M. *J. Am. Chem. Soc.* **1996**, *118*, 7551−7557. (b) Stubbe, J.; van der Donk, W. A. *Chem. Biol.* **1995**, *2*, 793−801.
(5) (a) Henriksen, M. A.; Cooperman, B. S.; Salem, J. S.; Li, L. S.; Rubin, H. *J. Am. Chem. Soc.* **1994**, *116*, 9773−9774. (b) Högbom, M.; Stenmark, P.; Voevodskaya, N.; McClarty, G.; Gräslund, A.; Nordlund, P. *Science* **2004**, *305*, 245−248. (c) Larsson, A.; Sjöberg, B. M. *EMBO J.* **1986**, *5*, 2037−2040. (d) Pötsch, S.; Lendzian, F.; Ingemarson, R.; Hornberg, A.; Thelander, L.; Lubitz, W.; Lassmann, G.; Graslund, A. *J. Biol. Chem.* **1999**, *274*, 17696−17704.

10.1021/ja050904q CCC: $30.25

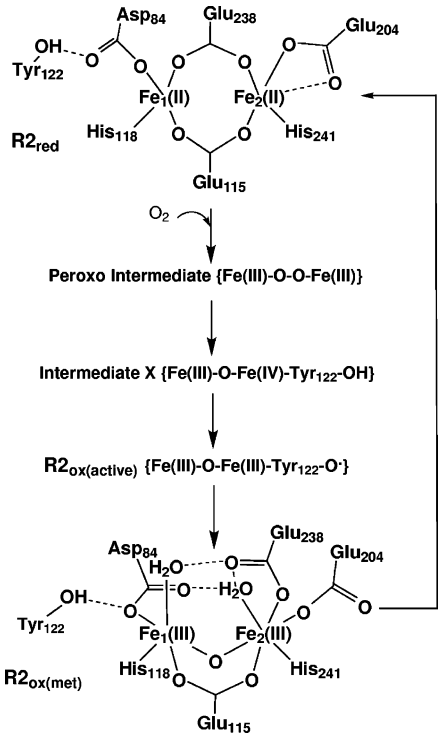

Figure 1. Schematic of the reaction cycle of formation of the active diferric cluster ($R2_{ox(active)}$) (with tyrosyl radical) from the reaction of O_2 with the diferrous cluster ($R2_{red}$). X is the intermediate state with an Fe(III)−O−Fe(IV) center.

in the active Fe(III)Fe(III)−Tyr−O• form (eq III), and subsequently, an additional cluster oxygen protonation is needed to obtain the reactant form of eq I, where $n = 2$. Presently, the structure for the active form of the protein that contains the tyrosine radical is unknown; however, X-ray structures of RNR from *E. coli* are available for both the reduced (red) and oxidized (ox) (met) forms (see Figure 1).[6,7] The diiron active sites of subunit R2 in reduced and oxidized forms have also been studied with density functional methods.[8]

In both the reduced and oxidized (met) states, Fe1 (which is close to Tyr122) is ligated to the side chains of Asp84 and His118, and the other iron (Fe2) is ligated to Glu204 and His241. In the diferrous cluster, both carboxylate groups from Glu238 and Glu115 exist in a bridging position between the two irons. In the diferric (met) center, the carboxylate of Glu238 changes from the bidentate position to monodentate binding with only Fe2, and each iron site has a binding terminal water molecule, which also H-bonds with Glu238 and/or Asp84.

Though much effort has been made both experimentally and theoretically,[4,9−21] there is limited knowledge about the stages of the catalytic cycle, that is, between the diferrous and diferric (met) forms, including how the O_2 molecule interacts with the Fe(II)Fe(II) center, how electron, proton, and oxygen species transfer within the active site, how the geometrical structures are rearranged, and how the active Tyr122•−Fe(III)Fe(III) cluster is formed. Very recently, on the basis of their analysis of the spectroscopic signatures of the R2−W48F/D84E biferric peroxo intermediate and density functional theory (DFT) geometry optimizations, Skulan et al. proposed that the O_2 molecule binds with the Fe(II)Fe(II) center in the *cis*-μ-1,2-peroxo form.[9b] As shown by ENDOR and Mössbauer hyperfine spectra,[10−17] after the O_2 binding and before the formation of active R2, a transient species (intermediate X) is formed which oxidizes tyrosine to the stable radical form, as shown in Figure 1.

Although there has been a significant experimental attempt to elucidate the structure of this short-lived catalytic species, the detailed structure of intermediate X is still not clear.[4a,10−17] A combination of Q-band ENDOR and Mössbauer data on Y122F−R2 indicates that the iron centers of X are high-spin Fe(III) ($S = {}^5/_2$) and high-spin Fe(IV) ($S = 2$) sites that antiferromagnetically couple to give an $S_{total} = {}^1/_2$ ground state.[4a] The best-fit Mössbauer isomer shifts and quadrupole splittings on Fe were redetermined on the basis of accurate ^{57}Fe ENDOR hyperfine parameters as constraints. X is therefore presently described as a spin-coupled Fe(III)Fe(IV) center without a radical, but with significant spin delocalization onto the oxygen ligand(s).[4a] All experimental data support the existence of at least one μ-oxo bridge in the core structure of X.[9a,12−17] A short Fe−Fe distance of 2.5 Å for X is implicated by the EXAFS measurements and data analysis for both wild-type and mutant Y122F proteins.[15] On the basis of this very short Fe−Fe distance, several possible core structures for X were proposed, each of which includes at least one μ-oxo bridge and two monodentate or/and bidentate carboxylate bridges from Glu115 and Glu238.[15,17] Very recently, on the basis of their CW and pulsed Q-band ^{17}O-ENDOR experiments on Y122F−R2 and the former ENDOR[14] and EXAFS[15] observations, Burdi et al.[16] proposed a structure for X which contains two oxygen atoms,

(6) (a) Nordlund, P.; Sjöberg, B. M.; Eklund, H. *Nature* **1990**, *345*, 593−598. (b) Nordlund, P.; Eklund, H. *J. Mol. Biol.* **1993**, *232*, 123−164. (c) Nordlund, P.; Eklund, H. *Curr. Opin. Struct. Biol.* **1995**, *5*, 758−766.
(7) Logan, D. T.; Su, X. D.; Åberg, A.; Regnström, K.; Hajdu, J.; Eklund, H.; Nordlund, P. *Structure* **1996**, *4*, 1053−1064.
(8) (a) Lovell, T.; Li, J.; Noodleman, L. *Inorg. Chem.* **2001**, *40*, 5251−5266. (b) Lovell, T.; Li, J.; Noodleman, L. *J. Biol. Inorg. Chem.* **2002**, *7*, 799−809. (c) Lovell, T.; Himo, F.; Han, W.-G.; Noodleman, L. *Coord. Chem. Rev.* **2003**, *238*−*239*, 211−232. (d) Noodleman, L.; Lovell, T.; Han, W.-G.; Liu. T.; Torres, R. A.; Himo, F. In *Comprehensive Coordination Chemistry II: From Biology to Nanotechnology*; Lever, A. B. P., Ed.; Elsevier: Philadelphia, 2003; Vol. 2, pp 491−510.
(9) (a) Mitic, N.; Saleh, L.; Schenk, G.; Bollinger, J. M., Jr.; Solomon, E. I. *J. Am. Chem. Soc.* **2003**, *125*, 11200−11201. (b) Skulan, A. J.; Brunold, T. C.; Baldwin, J.; Saleh, L.; Bollinger, J. M., Jr.; Solomon, E. I. *J. Am. Chem. Soc.* **2004**, *126*, 8842−8855.
(10) (a) Bollinger, J. M., Jr.; Edmondson, D. E.; Huynh, B. H.; Filley, J.; Norton, J. R.; Stubbe, J. *Science* **1991**, *253*, 292−298. (b) Bollinger, J. M., Jr.; Stubbe, J.; Huynh, B. H.; Edmondson, D. E. *J. Am. Chem. Soc.* **1991**, *113*, 6289−6291. (c) Bollinger, J. M., Jr.; Tong, W. H.; Ravi, N.; Huynh, B. H.; Edmondson, D. E.; Stubbe, J. *J. Am. Chem. Soc.* **1994**, *116*, 8015−8023; 8024−8032. (d) Baldwin, J.; Krebs, C.; Ley, B. A.; Edmondson, D. E.; Huynh, B. H.; Bollinger, J. M., Jr. *J. Am. Chem. Soc.* **2000**, *122*, 12195−12206. (e) Krebs, C.; Chen, S.; Baldwin, J.; Ley, B. A.; Patel, U.; Edmondson, D. E.; Huynh, B. H.; Bollinger, J. M., Jr. *J. Am. Chem. Soc.* **2000**, *122*, 12207−12219.
(11) Ravi, N.; Bollinger, J. M., Jr.; Huynh, B. H.; Edmondson, D. E.; Stubbe, J. *J. Am. Chem. Soc.* **1994**, *116*, 8007−8014.
(12) Burdi, D.; Sturgeon, B. E.; Tong, W. H.; Stubbe, J.; Hoffman, B. M. *J. Am. Chem. Soc.* **1996**, *118*, 281−282.
(13) Veselov, A.; Scholes, C. P. *Inorg. Chem.* **1996**, *35*, 3702−3705.
(14) Willems, J. P.; Lee, H. I.; Burdi, D.; Doan, P. E.; Stubbe, J.; Hoffman, B. M. *J. Am. Chem. Soc.* **1997**, *119*, 9816−9824.
(15) Riggs-Gelasco, P. J.; Shu, L.; Chen, S.; Burdi, D.; Huynh, B. H.; Que, L., Jr.; Stubbe, J. *J. Am. Chem. Soc.* **1998**, *120*, 849−860.
(16) Burdi, D.; Willems, J. P.; Riggs-Gelasco, P. J.; Antholine, W. E.; Stubbe, J.; Hoffman, B. M. *J. Am. Chem. Soc.* **1998**, *120*, 12910−12919.
(17) Hsu, H. F.; Dong, Y.; Shu, L.; Young, V. G., Jr.; Que, L., Jr. *J. Am. Chem. Soc.* **1999**, *121*, 5230−5237.
(18) (a) Siegbahn, P. E. M. *Inorg. Chem.* **1999**, *38*, 2880−2889. (b) Siegbahn, P. E. M. *Chem. Phys. Lett.* **2002**, *351*, 311−318. (c) Siegbahn, P. E. M. *Q. Rev. Biophys.* **2003**, *36*, 91−145.
(19) Han, W.-G.; Lovell T.; Liu, T.; Noodleman, L. *Inorg. Chem.* **2003**, *42*, 2751−2758.
(20) Noodleman, L.; Lovell T.; Han, W.-G.; Li, J.; Himo, F. *Chem. Rev.* **2004**, *104*, 459−508.
(21) Han, W.-G.; Lovell T.; Liu, T.; Noodleman, L. *Inorg. Chem.* **2004**, *43*, 613−621.

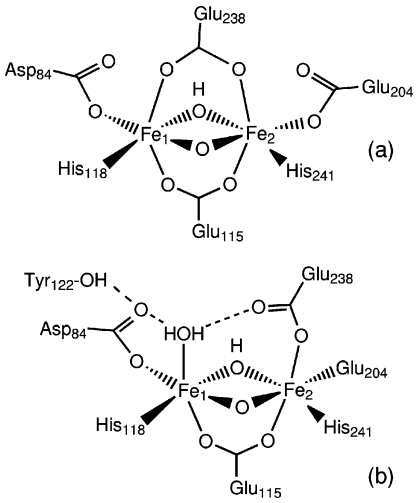

Figure 2. Two RNR−X active site structure models suggested by Siegbahn.[18a,c] Model (a) has also been examined in our first study of proposed RNR−X-type species.[19,20]

both initially derived from O_2, with one present as a μ-oxo bridge and one as a terminal aqua ligand (the latter may exchange with solvent) bound to the Fe(III) site; one or two additional mono-oxygen bridges provided by the carboxylate oxygens of Glu115 and Glu238 may also be present. Data analysis of the spin-allowed Fe(IV) d−d transitions for Y122F−R2 also favored the mono-μ-oxo model for X compared with rapid freeze−quench magnetic circular dichroism (RFQ-MCD) results.[9a]

On the basis of DFT calculations, Siegbahn has proposed two models for the active site of intermediate X (see Figure 2).[18a,c] His first model is shown in Figure 2a (also see Figure 6 in ref 18a), which contains one μ-oxo bridge, one hydroxo bridge, and two bidentate carboxylates from Glu115 and Glu238. Following geometry optimization of this $S_{total} = {}^1/_2$ model using the B3LYP DFT approach,[18a] an Fe−Fe distance of 2.61 Å was obtained. Furthermore, spin populations of 0.99 and −1.71 were noted for the two iron sites. Such small spin populations are more characteristic of low-spin and intermediate-spin Fe centers, rather than high-spin Fe sites, and appear inconsistent with the ENDOR and Mössbauer data for X. Siegbahn's second model (Figure 2b, also see Figure 12 in ref 18c) contains one μ-oxo bridge, one hydroxyl bridge, and one terminal water.[18c] The oxidation state was suggested to be Fe1(IV)Fe2(III).[18c] No other detailed property information has been presented yet for this model.

In our first study of proposed RNR−X-type species, we have examined Siegbahn's first and related models (Figure 3 in ref 19) using broken-symmetry DFT and spin-projection methods.[19,20] Some important second- and third-shell H-bonding partners have also been included in the active site quantum cluster, and both high-spin and intermediate-spin states have been examined, along with Fe(III) ↔ Fe(IV) valence interchange between Fe1 and Fe2. Our study showed that this model exhibits an energetic preference for a bridging hydroxide rather than a terminal hydroxide or water molecule. The lowest-energy structure we obtained displays an Fe−Fe distance of 2.708 Å and intermediate-spin AF-coupled Fe centers with $S_{Fe1} = {}^3/_2$ and $S_{Fe2} = 1$. The intermediate-spin AF coupling conflicts with the high-spin Fe sites indicated by ^{57}Fe hyperfine spectra. Also, Mössbauer property calculations for three different spin states

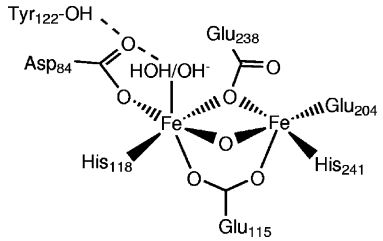

Figure 3. RNR−X active site model which was examined in our second study of proposed RNR−X-type species.[21]

of lowest energy for this model produce very similar isomer shift values for Fe1 and Fe2. This contrasts with the experimental situation in which the two iron sites can be clearly distinguished on the basis of their different isomer shift parameters. Further, for the two lowest-energy states $\{S_{Fe1} = {}^3/_2, S_{Fe2} = 1\}$ and $\{S_{Fe1} = 2, S_{Fe2} = {}^5/_2\}$ (AF-coupled), the calculated isomer shift and quadrupole splitting values of the Fe(IV) center are larger than the corresponding ones for the Fe(III) site, which is also inconsistent with the experimental data. On this basis, we therefore concluded that the model which contains two bidentate carboxylate groups, a bridging μ-oxo, and a bridging hydroxide is unlikely to be the core structure of X.[19]

In our second study[21] on proposed RNR−X-type species, we have examined a model which closely followed the structure for RNR−X proposed by Burdi et al.[16] The core structure of this model is shown in Figure 3 (also see Figure 2 in ref 21). It contains a single oxo bridge, one terminal H_2O or OH^- ligand, a bidentate carboxylate from Glu115, and a mono-oxygen bridge provided by Glu238. The diiron centers were assigned as high-spin Fe(III)Fe(IV) antiferromagnetically coupled to give the $S_{total} = {}^1/_2$ ground state. Both the Fe1(III)Fe2(IV) and Fe1(IV)Fe2(III) states were examined. Calculations show that the model with a terminal hydroxide in the antiferromagnetic Fe1(IV)Fe2(III)$\{S_{Fe1} = 2, S_{Fe2} = {}^5/_2\}$ state is the lowest-energy state. However, the predicted ^{1}H proton and ^{17}O hyperfine tensors for this state do not show good agreement with the experiments. The calculated Fe1−Fe2 distances for this and the other three clusters are >2.9 Å, much longer than the 2.5 Å which was predicted by the EXAFS measurements. The mono-oxygen bridge provided by Glu238 tends to be closer to one of the Fe sites in all clusters and does not function effectively as a bridge in helping to produce a short Fe−Fe distance. Overall, the models in our second study are also not likely to represent the core structure of RNR intermediate X. The model with the terminal OH^- binding to the Fe1(III) center, however, shows the best calculated ^{1}H proton and ^{17}O hyperfine tensors compared with the experimental values. This supports the earlier proposal, based on analysis of ENDOR spectra (Willems et al.[14]), that the terminal hydroxide or water binds to the Fe(III) site in RNR−X. In the work reported in ref 21, we did not perform Mössbauer and hyperfine calculations on the structure with a terminal water in the Fe1(III)Fe2(IV) state, since it is at higher energy than the Fe1(IV)Fe2(III) state and the pK_a calculations show that the terminal hydroxide forms of this model are more favored in a polar environment.[21] To complete the calculations for our second study and also to be able to compare with the models in the current study, we have performed the Mössbauer and hyperfine calculations for the large model cluster (see Figure 2 of ref 21) with a terminal

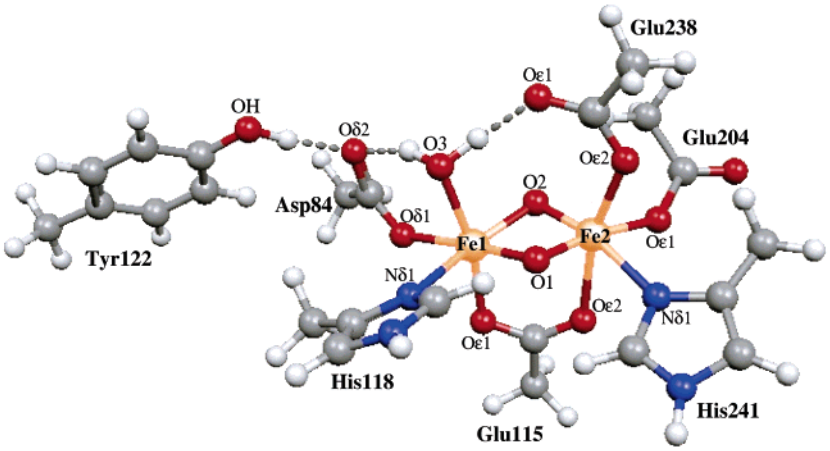

Figure 4. Model I of RNR−X studied in the present paper, proposed to represent the active site structure of class I RNR intermediate X. The corresponding Y122F (Tyr122 → Phe122 mutant) cluster is similar to this structure, but with the change of the OH group in Tyr122 to H.

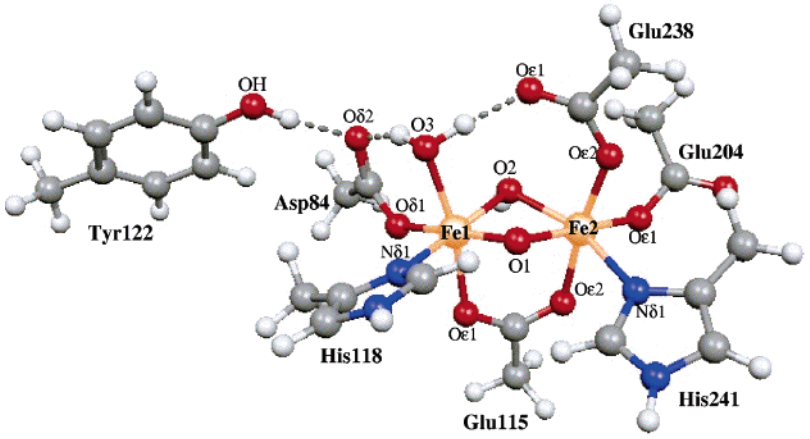

Figure 5. Second model (model II) for the RNR−X active site structure studied in the present paper. The corresponding Y122F cluster (changing the OH group in Tyr122 to H) is also studied here.

water in the Fe1(III)Fe2(IV) state. This structure will be called X_{2nd}\{Fe1(III)Fe2(IV)−$(H_2O)_t$\} hereafter. The results will be given in Table 3.

In this paper, we continue the study of proposed RNR−X-type species. Three new models are examined here. We have learned from our previous studies that RNR−X is unlikely to have two bidentate carboxylate groups, that a mono-oxygen bridge provided by the carboxylate group is also unlikely to exist, and that without a second μ-oxo or hydroxyl bridge, the very short Fe−Fe distance (2.5 Å) which was predicted by the EXAFS measurements[15] is also unlikely to be reproduced. Therefore, our first model (model I; see Figure 4) in this study contains two μ-oxo bridges, one terminal water which binds to Fe1, and one bidentate carboxylate group from Glu115. The conformations of the terminal water and the carboxylate group of Glu238 are similar to those in the oxidized (met) form (see Figure 1). Model II is shown in Figure 5. It is exactly the second RNR−X model proposed by Siegbahn, except for a valence interchange of Fe1(IV)Fe2(III) to Fe1(III)Fe2(IV).[18c] In comparison to model I, the second μ-oxo bridge is replaced by a hydroxide. By calculating the pK_a of this hydroxyl group, we will predict whether model I or model II is the more stable intermediate state. Since only one bridging oxo and one terminal water (or hydroxide) were suggested in the experimentally derived core structure of RNR−X proposed by Burdi et al.,[16] in our model III (Figure 6) we delete the second oxo or hydroxyl bridge to see if the properties of this structure will be better than those of model I and model II. Since most of the experiments were mainly performed on Y122F−R2, for all three models the corresponding mutant Y122F forms (the −OH group in Tyr122 is replaced by a hydrogen atom) are also studied and will be compared first with the experimental data. The diiron centers are constructed as high-spin Fe(III)Fe(IV) and antiferromagnetically coupled to give the $S_{total} = {}^1/_2$ ground state. To resolve the question of whether Fe1 or Fe2 is the ferric site, both the Fe1(III)Fe2(IV) and Fe1(IV)Fe2(III) states are examined. It will be shown that the ^{1}H and ^{17}O hyperfine coupling constants of the terminal water in the Fe1(III)Fe2(IV) state are much closer to experimental data than those in the Fe1(IV)Fe2(III) state. We therefore present only the Fe1(III)Fe2(IV) state calculations in the main text and put all the Fe1(IV)Fe2(III) state results in the Supporting Information. To be clear whether a terminal water or a terminal hydroxide is preferred in these three models, we also studied the terminal hydroxide form for the native-type models I, II, and III in the Fe1(III)Fe2(IV) state. The calculated properties for all the clusters of the three new models and X_{2nd}\{Fe1(III)Fe2(IV)−$(H_2O)_t$\}, including the core geometries, spin states, Mössbauer parameters (isomer shift and quadrupole splitting values), ^{57}Fe, ^{1}H, and ^{17}O hyperfine tensors, and estimations of the Fe(IV) d−d transition energies, are compared with the corresponding experimental results. In the following sections we will show that our

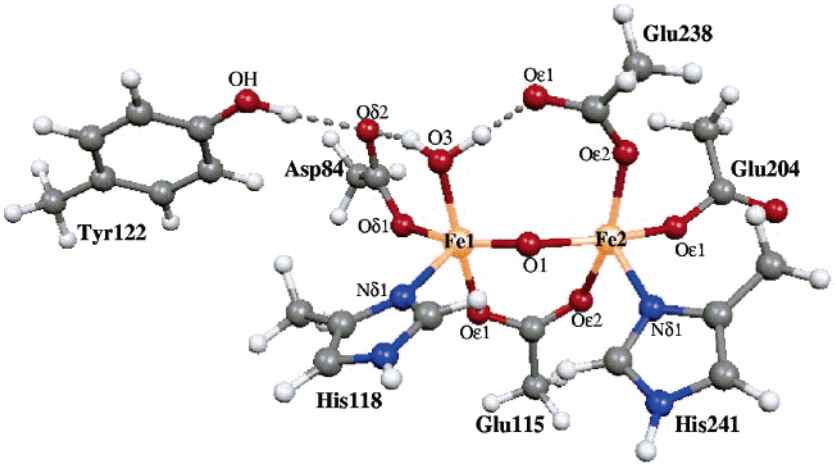

Figure 6. Third model (model III) for RNR−X active site structure studied in the present paper. The corresponding Y122F cluster is constructed by replacing the OH group in Tyr122 with H.

Fe1(III)Fe2(IV) state model I−$(H_2O)_t$ is the best among all the model complexes (including our previously studied ones) in predicting many of the experimentally observed properties for RNR−X. We therefore propose that this model represents the active site structure of class I RNR intermediate X.

2. Computational Methodology

2.1. Geometries and Energies. The initial positions of the first-shell ligand side chains in the model clusters were taken from chain A of the oxidized RNR (met) X-ray crystal structure (PDB code 1RIB)[6b] by breaking the $C_\beta-C_\alpha$ or $C_\gamma-C_\beta$ bonds and adding a linking hydrogen atom to fill the open valence of the terminal carbon atom.[22] As shown in Figures 4−6, these side chains are Asp84, His118, Glu115, His241, Glu204, and Glu238. The side chain of Tyr122 or Phe122 in Y122F is also included in the model clusters. The μ-oxo bridge (O1) which lies between His118 and His241 and the terminal water which binds with Fe1 in the active site of $R2_{ox}$ are maintained in our models. The additional oxygen (O2) which lies between Asp84 and Glu204 is added in our models I and II. The orientation of the Asp84 side chain is modified so that one of the oxygen atoms in the carboxylate group H-bonds to both the terminal water and Tyr122 in the native form of the models.

All density functional spin-unrestricted calculations have been performed using the Amsterdam Density Functional (ADF) packages.[23,24] For a simplified representation of stabilizing effects of the protein and solvent which generates a polar environment, the geometries of all protein model clusters were optimized using the COSMO (conductor-like screening model) solvation model in ADF with dielectric constant $\epsilon = 80.0$.[25,26] The COSMO model is a dielectric solvent continuum model in which the solute molecule is embedded in a molecular-shaped cavity surrounded by a dielectric medium with a given dielectric constant. In all calculations, the parametrization of Vosko, Wilk, and Nusair (VWN)[27] was used for the local density approximation term, and the corrections of Perdew and Wang (PW91)[28] were used for the nonlocal exchange and correlation terms. During geometry optimizations, we applied the triple-ζ plus polarization (TZP) basis set for the two iron sites and the double-ζ plus polarization (DZP) basis set for other atoms. The inner core shells of C(1s), N(1s), O(1s), and Fe(1s,2s,2p) were treated by the frozen core approximation. Mössbauer parameter and hyperfine coupling calculations were then performed on the optimized geometries using TZP basis set for all atoms without freezing the core electrons. The accuracy parameter for the numerical integration grid was set to 4.0.

Experimentally, X is assigned as an Fe(III)Fe(IV) $S_{total} = {}^1/_2$ ground state, and the two Fe sites are high spin and antiferromagnetically (AF) coupled.[4] We therefore performed geometry optimizations on two kinds of spin states, $\{S_1 = {}^5/_2, S_2 = -2\}$ and $\{S_1 = -2, S_2 = {}^5/_2\}$, for most of the clusters. (Note: Total spin quantum numbers cannot be negative. We use the negative sign simply to denote the AF coupling arrangement.)

Usually, the AF spin-coupled state cannot be obtained directly from the normal DFT calculations in ADF. As in previous work, we represent the AF spin-coupled state in DFT by a "broken-symmetry" state, where a spin-unrestricted determinant is constructed in which one of the Fe sites adopts majority spin-up electrons and the other site has majority spin-down electrons.[8,29−35] To obtain this broken-symmetry solution, first we construct a ferromagnetically (F) spin-coupled ($S_{max} =$

(22) Han, W.-G.; Tajkhorshid, E.; Suhai, S. *J. Biol. Struct. Dyn.* **1999**, *16*, 1019−1032.
(23) ADF2003.01 and ADF2004.01, SCM, Theoretical Chemistry, Vrije Universiteit, Amsterdam, The Netherlands (http://www.scm.com).
(24) (a) Fonseca Guerra, C.; Snijders, J. G.; te Velde, G.; Baerends, E. J. *Theor. Chem. Acc.* **1998**, *99*, 391−403. (b) te Velde, G.; Bickelhaupt, F. M.; Baerends, E. J.; Guerra, C. F.; van Gisbergen, S. J. A.; Snijders, J. G.; Ziegler, T. *J. Comput. Chem.* **2001**, *22*, 931−967. (c) van Lenthe, E.; van der Avoird, A.; Wormer, P. E. S. *J. Chem. Phys.* **1998**, *108*, 4783−4796.
(25) (a) Klamt, A.; Schrüümann, G. *J. Chem. Soc., Perkin Trans.* **1993**, *2*, 799−805. (b) Klamt, A. *J. Phys. Chem.* **1995**, *99*, 2224−2235. (c) Klamt, A.; Jones, V. *J. Chem. Phys.* **1996**, *105*, 9972−9981. (d) Pye, C. C.; Ziegler, T. *Theor. Chem. Acc.* **1999**, *101*, 396−408.
(26) (a) Liu, T.; Han, W.-G.; Himo, F.; Ullmann, G. M.; Bashford, D.; Toutchkine, A.; Hahn, K. M.; Noodleman, L. *J. Phys. Chem. A* **2004**, *108*, 3545−3555. (b) Han, W.-G.; Liu, T.; Himo, F.; Toutchkine, A.; Bashford, D.; Hahn, K. M.; Noodleman, L. *ChemPhysChem* **2003**, *4*, 1084−1094.
(27) Vosko, S. H.; Wilk, L.; Nusair, M. *Can. J. Phys.* **1980**, *58*, 1200−1211.
(28) Perdew, J. P.; Chekavry, J. A.; Vosko, S. H.; Jackson, K. A.; Perderson, M. R.; Singh, D. J.; Fioihais, C. *Phys. Rev. B* **1992**, *46*, 6671−6687.
(29) (a) Noodleman, L.; Case, D. A. *Adv. Inorg. Chem.* **1992**, *38*, 423−470. (b) Noodleman, L.; Chen, J.-L.; Case, D. A.; Giori, C.; Rius, G.; Mouesca, J.-M.; Lamotte, B. In *Nuclear Magnetic Resonance of Paramagnetic Macromolecules*; Kluwer Academic Publishers: Dordrecht, The Netherlands, 1995; pp 339−367. (c) Kuramochi, H.; Noodleman, L.; Case, D. A. *J. Am. Chem. Soc.* **1997**, *119*, 11442−11451. (d) Adams, D. A.; Noodleman, L.; Hendrickson, D. N. *Inorg. Chem.* **1997**, *36*, 3966−3984. (e) Case, D. A.; Noodleman, L.; Li, J. In *Metal−Ligand Interactions in Chemistry, Physics and Biology*; Russo, N., Salahub, D. R., Eds.; Kluwer Academic Publishers: Dordrecht, The Netherlands, 2000; pp 19−47. (f) Cheng, R.-J.; Chen, P.-Y.; Lovell, T.; Liu, T.; Noodleman, L.; Case, D. A. *J. Am. Chem. Soc.* **2003**, *125*, 6774−6783.
(30) Mouesca, J.-M.; Chen, J. L.; Noodleman, L.; Bashford, D.; Case, D. A. *J. Am. Chem. Soc.* **1994**, *116*, 11898−11914.
(31) Zhao, X. G.; Richardson, W. H.; Chen, J.-L.; Li, J.; Noodleman, L.; Tsai, H.-L.; Hendrickson, D. N. *Inorg. Chem.* **1997**, *36*, 1198−1217.
(32) Li, J.; Noodleman, L. In *Spectroscopic Methods in Bioinorganic Chemistry*; Solomon, E. I., Hodgson, K. O., Eds.; ACS Symposium Series 692; American Chemical Society: Washington, DC, 1998; Chapter 9, pp 179−195.
(33) (a) Lovell, T.; Li, J.; Noodleman, L. *Inorg. Chem.* **2001**, *40*, 5267−5278. (b) Lovell, T.; Torres, R. A.; Han, W.-G.; Liu, T.; Case, D. A.; Noodleman, L. *Inorg. Chem.* **2002**, *41*, 5744−5753. (c) Lovell, T.; Li, J.; Case, D. A.; Noodleman, L. *J. Biol. Inorg. Chem.* **2002**, *7*, 735−749.
(34) (a) Lovell, T.; Han, W.-G.; Liu, T.; Noodleman, L. *J. Am. Chem. Soc.* **2002**, *124*, 5890−5894. (b) Liu, T.; Lovell, T.; Han, W.-G.; Noodleman, L. *Inorg. Chem.* **2003**, *42*, 5244−5251; **2004**, *43*, 6858.

$S_{total} = {}^9/_2$) determinant, where the spins on both irons are aligned in a parallel fashion. We then rotate the spin vector located on either atom Fe1 or atom Fe2 by interchanging the α and β fit density blocks on the site Fe1 or Fe2 from the output file TAPE21 created by this F-coupled calculation in ADF. Using the modified TAPE21 as a restart file and reading the starting spin density from there, we then obtain the expected broken-symmetry state through single-point energy calculation or geometry optimization.

Typically, the spin Hamiltonian H for transition metal dimers (here Fe1 and Fe2) is expressed via the Heisenberg coupling constant J,

$$H = -2JS_1 \cdot S_2 \tag{1}$$

while for a completely delocalized mixed-valence dimer, a more general spin Hamiltonian is

$$H = -2J_0 S_1 \cdot S_2 \pm B(S_{total} + {}^1/_2) \tag{2}$$

where B is the resonance delocalization parameter.[30,31] If the total spin S_{total} is small and B is not large, the resonance stabilization energy $-B(S_{total} + {}^1/_2)$ is also small, and the resonance effects can be quenched by site and environmental effects including site coordination dissymmetry, solvation, counterions, and vibronic coupling which produce an asymmetry between the metal sites.[30,31] As in ref 19, we will ignore this resonance term when calculating the pure-spin ground-state energies. When a Heisenberg Hamiltonian (eq 1) is applicable, the energy difference between F-coupling ($S_{total} = S_{max} = S_1 + S_2$) and broken-symmetry (BS) ($S_{total} = S_{min} = |S_1 - S_2|$) states can be described by

$$E_F - E_{BS} = -4JS_1S_2 \tag{3}$$

Here, the high-spin energy (E_F) is obtained by a single-point energy calculation on the optimized broken-symmetry geometry (which has energy E_{BS}). J is then obtained from eq 3, and the pure-spin ground-state energy E_0 for the particular spin state (S_1, S_2) coupled to S_{min} according to the broken-symmetry geometry is estimated as

$$E_0 = E_F + JS_{max}(S_{max} + 1) - JS_{min}(S_{min} + 1) \tag{4}$$

The DFT broken-symmetry plus spin projection method has been successfully applied to study the geometric, energetic, pK_a, proton NMR shifts, optical, and Fe Mössbauer and ligand hyperfine properties of metal-containing protein active sites and complexes including the Fe(II)Fe(II) and Fe(III)Fe(III) state active site of RNR−R2 and the hydroxylase component of methane monooxygenase (MMOH), the Fe(IV)Fe(IV) intermediate state Q of MMOH, different oxidation states of 2Fe−2S, 4Fe−4S, and Mo−7Fe−9S systems, Fe(III)−porphyrin complexes, heme-containing peroxidase intermediates in horseradish peroxidase (HRP), and a Mn(III)Mn(IV) dimer complex.[8,29−35]

2.2. Mössbauer Isomer Shift and Quadrupole Splitting Calculations. The correlation between isomer shifts δ and Fe nuclear densities (electron densities at Fe nuclei) $\rho(0)$ is given by

$$\delta = \alpha(\rho(0) - 11884.0) + C \tag{5}$$

where the slope α and the intercept C need to be obtained from a linear correlation between measured isomer shifts and calculated electron densities from a group of sample iron complexes. Previously we have obtained $\alpha = -0.664 \pm 0.04$ and $C = 0.478 \pm 0.02$ mm s^{-1} through linear regression for a series of 15 dinuclear plus 6 polar mononuclear iron complexes in different (+2, +2.5, +3, +3.5) oxidation states.[34] The fitting gave a correlation coefficient ($r = -0.94$) with a standard deviation of 0.11 mm s^{-1}. However, only gas-phase calculations were performed directly on the geometries of the sample complexes taken from the Cambridge Structural Database (only the hydrogen atom positions were optimized). Though the geometries of these small molecules are of high resolution, they are not necessarily at the minimum on the potential energy surface of the specified PW91 potential. The gas-phase calculations also ignored solvation effects. We have now decided to optimize the complex geometries of our training set within the COSMO model with a reasonable polar environment, $\epsilon = 32.7$ (the dielectric constant for methanol). The basis set for each atom used in the optimization is exactly the same as described above. A single-point energy calculation was then performed on the geometry-optimized structure using the all-electron TZP basis set for each atom type, and the electron densities at the iron nuclei were calculated using our program HYPERS-2000.[34b] We also noticed a problem with our previous fitting (see Figure 1 and Table 1 of ref 34b), where the Fe(II) (with $\delta > 1.0$ mm s^{-1}) and Fe(III) sites ($\delta < 0.65$ mm s^{-1}) are separated and far from each other. Eight out of nine Fe(II) points are above the fitting line, most of the Fe(III) sites are below the line, and the Fe(+3.5) sites on the right end are above the line. Therefore, with this global fitting, our isomer shift predictions end up underestimating the Fe(II) and Fe(IV or +3.5) sites but in general overestimating the Fe(III) state. This is the reason we predicted very large isomer shift values for the oxidized met RNR−R2 and oxidized MMO (methane monooxygenase) compared with the experimental data (see Tables 3 and 4 in ref 34b). Our hypothesis is that the electron-rich ferrous Fe is much more sensitive than Fe(III) and Fe(IV) to its ligands and solvent (counterion) environment. There is possible charge transfer from the Fe(II) center (involving the first-shell ligands) to the environment, which cannot be calculated even using the COSMO solvation model. The shift of the electron density at Fe(II) nuclei is therefore underestimated. To reasonably predict the ^{57}Fe isomer shifts in different oxidation state, one needs to fit the parameters separately for Fe(II) and Fe(III,IV) complexes.

We have redone the linear regression for all the Fe$^{2.5+,3+,3.5+}$ complexes described in Table 1 of ref 34b, plus three new Fe(IV) complexes, Fe(OEC)Cl {$S = 1$, $\delta = 0.22$ mm s^{-1} at 4.2 K},[36a] Fe(OEC)C$_6$H$_5$ {$S = 1$, $\delta = -0.08$ mm s^{-1} at 4.2 K },[36a] and FeCl(η^4-MAC*)$^-$ {$S = 2$, $\delta = -0.04$ mm s^{-1} at 4.2 K}.[36b] The electron densities at Fe nuclei now were calculated at the COSMO-optimized geometries. The new fitting parameters for Fe(III) and Fe(IV) complexes (in total 30 Fe sites) are $\alpha = -0.393 \pm 0.030$ and $C = 0.478 \pm 0.014$ mm s^{-1}. The correlation coefficient is $r = -0.929$, with a standard deviation SD = 0.077 mm s^{-1}. The names of the sample Fe complexes, their oxidation states, and the experimental and calculated isomer shifts can be found in the Supporting Information, Table S1. With the new parameters, we now predict the isomer shifts of the diferric state active site of MMOH to be 0.47 and 0.50 mm s^{-1}, which are in very good agreement with the experimental values of 0.50 and 0.51 mm s^{-1}.[37a] Similarly, the predictions for the isomer shifts of the met-diferric RNR−R2 active site, 0.53 and 0.58 mm s^{-1}, are also consistent with the observed values of 0.45 and 0.55 mm s^{-1}.[37b] Again, the geometries of the active site of the oxidized MMOH and RNR−R2 were optimized using the COSMO solvation model. In this paper, we will use the new linear equation, that is

$$\delta = -0.393(\rho(0) - 11884.0) + 0.435 \text{ mm s}^{-1} \tag{6}$$

to predict the isomer shifts of our new RNR−X COSMO-optimized models.

(35) (a) Sinnecker, S.; Neese, F.; Noodleman, L.; Lubitz, W. *J. Am. Chem. Soc.* **2004**, *126*, 2613−2622. (b) Noodleman, L.; Baerends, E. J. *J. Am. Chem. Soc.* **1984**, *106*, 2316−2327.

(36) (a) Vogel, E.; Will, S.; Tilling, A. S.; Neumann, L.; Lex, J.; Bill, E.; Trautwein, A. X.; Wieghardt, K. *Angew. Chem., Int. Ed. Engl.* **1994**, *33*, 731−735. (b) Kostka, K. L.; Fox, B. G.; Hendrich, M. P.; Collins, T. J.; Rickard, C. E. F.; Wright, L. J.; Münck, E. *J. Am. Chem. Soc.* **1993**, *115*, 6746−6757.

(37) (a) Fox, B. G.; Hendrich, M. P.; Surerus, K. K.; Andersson, K. K.; Froland, W. A.; Lipscomb, J. D.; Münck, E. *J. Am. Chem. Soc.* **1993**, *115*, 3688−3701. (b) Lynch, J. B.; Juarez-Garcia, C.; Münck, E.; Que, L. J., Jr. *Biol. Chem.* **1989**, *264*, 8091−8096. (c) Martínez-Pinedo, G.; Schwerdtfeger, P.; Caurier, E.; Langanke, K.; Nazarewicz, W.; Söhnel, T. *Phys. Rev. Lett.* **2001**, *87*, 062701(1−4).

To predict the quadrupole splittings (ΔE_Q), the electric field gradient (EFG) tensors (**V**) were calculated using the all-electron TZP basis set for all atom types at the COSMO-optimized geometries. **V** is diagonalized and its eigenvalues are reordered so that $|V_{zz}| \geq |V_{xx}| \geq |V_{yy}|$. η is then defined as

$$\eta = |(V_{xx} - V_{yy})/V_{zz}| \quad (7)$$

Finally, the quadrupole splitting for ^{57}Fe of the nuclear excited state ($I = {}^3/_2$) can be calculated as

$$\Delta E_Q = {}^1/_2 eQV_{zz}(1 + \eta^2/3)^{1/2} \quad (8)$$

where e is the electrical charge of a positive electron and Q is the nuclear quadrupole moment (0.15 barn) of Fe.[37c]

We have recalculated (see Table S2 and Figure S1) the quadrupole splittings at the COSMO-optimized geometries of all complexes given in Table 1 of ref 34b plus the three Fe(IV) complexes mentioned above (in total 39 Fe sites). The linear correlation between the calculated and the observed ΔE_Q absolute values (the experimental sign was not reported for many of these complexes), based on the equation

$$|\Delta E_{Q(exp)}| = A|\Delta E_{Q(cal)}| + B \quad (9)$$

gives a slope A which is almost the ideal value 1.0 ($A = 1.014 \pm 0.042$), and the intercept B is almost zero ($B = 0.009 \pm 0.075$ mm s^{-1}). The correlation coefficient is $r = 0.969$, with standard deviation SD = 0.254 mm s^{-1}. Overall, our predictions of the quadrupole splittings for these relatively small complexes are in very good agreement with the experimental data. The quality of our Mössbauer isomer shift fits and the calculated quadrupole splittings as well are very similar to those obtained independently by the Neese and Oldfield groups (comparing standard deviations, correlation coefficients, and the slope of the isomer shift) for different sets of complexes.[38] We also recalculated the quadrupole splittings for the COSMO-optimized met-diferric state RNR−R2 active site structure, and obtained −1.70 ($\eta = 0.41$) and −1.26 ($\eta = 0.26$) mm s^{-1} for the two Fe(III) sites. The corresponding experimental results are −2.44 ($\eta = 0.2$) and −1.62 ($\eta = 0.6$) mm s^{-1}.[37b] Though we underestimate the absolute values of these two sites, the signs and the relative electronic asymmetry are reproduced.

2.3. Hyperfine A-Tensor Calculations. To predict the ^{57}Fe, ^{1}H, and ^{17}O hyperfine coupling constants, we performed **A**-tensor calculations based on computed electronic spin densities using ADF.[24c] The **A**-tensor output from ADF is based on the assumption that there is only one unpaired electron in the system. Also, spin−orbit coupling contributions to the **A**-tensor are neglected, which is probably reasonable, but not perfect for high-spin Fe(III) and Fe(IV). For the present systems with high-spin AF-coupled sites, we therefore need to rescale the ADF-obtained **A**-tensors by the spin projection coupling factors $|K_A/2S_A|$ for Fe(III) ($K_A = {}^7/_3$, $S_A = {}^5/_2$) and $|K_B/2S_B|$ for Fe(IV) ($K_B = -{}^4/_3$, $S_B = 2$).[21,29b,35a] Absolute values of the coupling factors are used here, since the broken-symmetry state carries the proper **A**-tensor sign but not the correct magnitude (derived from the Wigner−Eckart theorem, vector coupling model). For the terminal OH^- or H_2O group, the coupling factors are determined by whether Fe1 is a ferric or ferryl center. For the bridging oxo or hydroxide, the coupling factor in this paper is taken as the average of $|K_A/2S_A|$ and $|K_B/2S_B|$.

2.4. pK_a Calculations. To examine whether model I or model II is favored, and whether a terminal H_2O or terminal hydroxide is favored in these three models, we need to calculate the pK_a values for the bridging $-OH^-$ or the terminal $-H_2O$ ligand (L) forms.

Taking the terminal water form as an example,

$$L(H_2O) \rightarrow L(OH^-) + H^+ \quad (10)$$

the pK_a value for the L(H_2O) cluster can be calculated by

$$1.37pK_a = E[L(OH^-)] - E[L(H_2O)] + E(H^+) + \Delta G_{sol}(H^+,1\text{ atm}) - T\Delta S_{gas}(H^+) + \Delta ZPE + {}^5/_2 RT \quad (11)$$

where E[L(OH^-)] and E[L(H_2O)] represent the energies (from the all-electron, all-TZP solvated single-point energy calculations on the COSMO-optimized geometries) for the active site clusters with ligand $-OH^-$ and $-H_2O$, respectively; $E(H^+) = 12.51567$ eV is the calculated energy of a spin-restricted proton obtained from gas-phase DFT calculation; and $\Delta G_{sol}(H^+,1\text{ atm}) = -262.11$ kcal/mol is the solvation free energy of a proton at 1 atm pressure. This term is obtained using very recent experimental results and is different from the value we used previously (−260.5 kcal/mol).[39−42] The very recent experimental values (involving also theoretical/computational analysis) for the free energy of hydration for H^+ have been reported to be around $\Delta G_{sol}(H^+,1\text{ M}) = -264.0$ kcal/mol, when the standard state is 1 M.[43] Therefore, we have

$$\Delta G_{sol}(H^+,1\text{ atm}) = \Delta G_{sol}(H^+,1\text{ M}) + RT\ln(24.46) = -262.11\text{ kcal/mol} \quad (12)$$

The translation entropy contribution to the gas-phase free energy of a proton is taken as $-T\Delta S_{gas}(H^+) = -7.76$ kcal/mol at 298 K and 1 atm pressure.[42] Finally, for better estimating the zero-point energy difference term, ΔZPE, we performed gas-phase geometry optimizations on the very simple active site models (changing the His side chains to $-NH_3$, replacing the Try122 by H_2O, and replacing the methyl groups by H) at the Fe1(III)Fe2(IV) state models I and II, and then applied frequency calculations. We will therefore use $\Delta ZPE = -6.31$ kcal/mol for calculating the pK_a of the bridging hydroxyl group for the process of (model II → model I + H^+), and $\Delta ZPE = -7.31$ kcal/mol for the processes of {L(H_2O) → L(OH^-) + H^+} in models I, II, and III (deprotonation of the terminal water ligand).

3. Results and Discussion

The Fe−Fe and Fe−O distances (Å), pK_a values, net spin populations, and Heisenberg J values (cm^{-1}) for all models in the Fe1(III)Fe2(IV)$\{S_1 = {}^5/_2, S_2 = -2\}$ state are given in Table 1.

The net spin populations are the main indication of the high-spin or intermediate-spin character of the Fe sites. In the ideal ionic limit, the net unpaired spin populations are 5 and 4 for the high-spin Fe(III) (five d-electrons) and Fe(IV) (four d-electrons) sites, respectively. The absolute calculated net spins in Table 1 for all model clusters are smaller (by about 1 e$^-$) than the ionic limit, indicative of substantial Fe−ligand covalency and consistent with previous results in related complexes, including $R2_{ox}$(met).[8,19,21] The opposite signs for the spin densities of Fe1 and Fe2 confirm the AF coupling.

(38) (a) Neese, F. *Inorg. Chim. Acta* **2002**, *337*, 181−192. (b) Neese, F. *Curr. Opin. Chem. Biol*. **2003**, *7*, 125−135. (c) Godbout, N.; Havlin, R.; Salzmann, R.; Debrunner, P. G.; Oldfield, E. *J. Am. Chem. Soc*. **1998**, *102*, 2342−2350. (d) Havlin, R.; Godbout, N.; Salzmann, R.; Wojdelski, M.; Arnold, W.; Schulz, C. E.; Oldfield, E. *J. Am. Chem. Soc.* **1998**, *120*, 3144−3151. (e) Zhang, Y.; Mao, J.; Oldfield, E. *J. Am. Chem. Soc*. **2002**, *124*, 7829−7839.

(39) (a) Richardson, W. H.; Peng, C.; Bashford, D.; Noodleman, L.; Case, D. A. *Int. J. Quantum Chem*. **1997**, *61*, 207−217. (b) Li, J.; Fisher, C. L.; Konecny, R.; Bashford, D.; Noodleman, L. *Inorg. Chem*. **1999**, *38*, 929−939. (c) Huang, H.; Han, W.-G.; Noodleman, L.; Grynszpan, F. *Bioorg. Med. Chem*. **2001**, *9*, 3185−3195. (d) Han, W.-G.; Lovell, T.; Noodleman, L. *Inorg. Chem*. **2002**, *41*, 205−218.

(40) Noyes, R. M. *J. Am. Chem. Soc*. **1962**, *84*, 512−522.

(41) Reiss, H.; Heller, A. *J. Phys. Chem*. **1985**, *89*, 4207−4213.

(42) Tawa, G. J.; Topol, I. A.; Burt, S. K.; Caldwell, R. A.; Rashin, A. A. *J. Chem. Phys*. **1998**, *109*, 4852−4863.

(43) (a) Liptak, M. D.; Shields, G. C. *J. Am. Chem. Soc*. **2001**, *123*, 7314−7319. (b) Palascak, M. W.; Shields, G. C. *J. Phys. Chem. A* **2004**, *108*, 3692−3694.

Table 1. Geometries (Å), pK_a Values, Net Spin Populations, and Heisenberg J Values (cm^{-1}) for RNR−X Active Site Models I, II, and III with Terminal H_2O, $(H_2O)_t$, or Terminal OH^-, $(OH^-)_t$ (Figures 4−7), with Native and Y122F Mutant Types in the Fe1(III)Fe2(IV){$S_1 = {}^5/_2$, $S_2 = -2$} State

	$(H_2O)_t$						$(OH^-)_t$		
model:	I		II		III		I	II	III
type:	Y122F	native	Y122F	native	Y122F	native	native	native	native
				Geometry					
Fe1−Fe2	*2.703*[a]	*2.688*[a]	2.848	2.843	3.182	3.196	2.737	2.869	3.122
Fe1−O1	1.911	1.901	1.864	1.851	1.738	1.812	1.951	1.794	1.792
Fe2−O1	1.742	1.747	1.726	1.731	1.725	1.722	1.749	1.771	1.745
Fe1−O2	1.927	1.923	2.093	2.101			1.942	2.237	
Fe2−O2	1.766	1.762	1.933	1.929			1.753	1.882	
Fe1−O3	2.087	2.093	2.023	2.028	1.935	2.016	1.853	1.809	1.807
			pK_a {$(OH^-)_{br,model\ II} \rightarrow (O^{2-})_{br,model\ I} + H^+$}						
	4.02	2.51							
			pK_a {$(H_2O)_t \rightarrow (OH^-)_t + H^+$}						
							13.20	7.38	7.60
				Net Spin Population					
Fe1	3.870	3.861	3.819	3.815	3.457	3.918	3.831	3.433	3.533
Fe2	−2.969	−2.964	−2.954	−2.944	−2.717	−2.988	−2.919	−2.716	−2.842
O1	−0.001	0.024	−0.087	−0.065	0.101	−0.022	−0.047	−0.006	−0.003
O2	0.016	0.013	0.052	0.059			−0.039	0.035	
O3	0.059	0.056	0.088	0.084	0.073	0.110	0.195	0.235	0.270
				J Values					
	−186.5	−190.3	−199.8	−199.2	−229.3	−180.7	−196.3	−306.0	−239.5

[a] The Fe−Fe distances obtained from model I in both native and Y122F types with terminal H_2O in the Fe1(III)Fe2(IV) state are the best compared with the experimental value of 2.5 Å obtained from EXAFS measurements and data analysis (ref 15).

Since only EXAFS measurements were reported for both wild-type and mutant Y122F R2 proteins, and most of the other experiments (Mössbauer, ENDOR, and MCD) were performed and reported mainly for the mutant Y122F protein, we will first focus on our calculated properties of the Y122F-type clusters and compare them with the experimental data and then with the calculated results for the native-type models. The calculated and the available experimental data of Fe nuclear densities (ρ(0)), isomer shifts (δ), quadrupole splittings (ΔE_Q), η, and ^{57}Fe, ^{1}H, and ^{17}O hyperfine couplings (rescaled by the spin coupling factors) for the Y122F-type models I, II, and III in the Fe1(III)Fe2(IV){$S_1 = {}^5/_2$, $S_2 = -2$} state are given in Table 2.

3.1. Y122F-Type Models I, II, and III with Terminal H_2O in the Fe1(III)Fe2(IV) State. The COSMO-optimized Fe−Fe distance of model I (2.703 Å) is by 0.15 and 0.48 Å (see Table 1), respectively, shorter than those in models II and III, and is the closest to 2.5 Å which was obtained from the EXAFS measurements and data analysis.[15] The isomer shifts (Table 2) of model I (0.56 (Fe1) and 0.22 (Fe2) mm s^{-1}) are also in excellent agreement with the experimental data (0.56 and 0.26 mm s^{-1}), and are much better than those of models II and III. Model III, though constructed closely following the proposed active site structure for RNR−X based on ENDOR, has the worst isomer shifts and longest Fe−Fe distance among these three models.[16]

The observed quadrupole splitting for Fe(IV) is −0.6 mm s^{-1}, with $\eta = 2.7$ (so $\eta > 1$). If we trace back and reorder the eigenvalues to have $|V_{zz}| \geq |V_{xx}| \geq |V_{yy}|$, we obtain ΔE_Q\{(Fe(IV)\}$_{exp} = 0.6$ mm s^{-1}, with $\eta = 0.08$, according to eqs 7 and 8. None of the calculated ΔE_Q results for these three models are consistent with the experimental data. However, only model I yields the correct relative absolute values of $|\Delta E_Q\{(Fe(III)\}| > |\Delta E_Q\{(Fe(IV)\}|$, which is in agreement with the experiment. Model III clearly gives the worst value for the $|\Delta E_Q\{(Fe(IV)\}|$ (1.50 mm s^{-1}).

Next, we compare the ^{1}H and ^{17}O hyperfine constants for the terminal water. The experimentally observed two ^{1}H proton hyperfine constants on the terminal water are excellently reproduced by our calculations for all three models (see H_{t1} and H_{t2}). Again, model I is the best among them, with nearly zero isotropic values (A^{iso}). Further, the experimentally observed ^{17}O hyperfine constants for the terminal oxygen (O_t) are also reproduced very well (see O3) by these three models (model III is worse than models I and II by comparison of the anisotropic components). Note that, experimentally, only the relative sign of the three principal values for ^{17}O **A**-tensors were determined, but the absolute signs were unknown.[16] So we have set the overall signs of the experimental ^{17}O **A**-tensors according to our corresponding calculations, respecting the relative signs set by experiment.

To examine whether the terminal water is ligated to an Fe(III) or Fe(IV) site, we also performed the same calculations for models I and II in the Fe1(IV)Fe2(III){$S_1 = -2$, $S_2 = {}^5/_2$} state. The corresponding results are given in the Supporting Information, Tables S3−S5. If the terminal water binds to Fe1(IV), the calculated ^{1}H and ^{17}O hyperfine constants for the water molecule are all too small in comparison with the experimental values. We therefore draw the conclusion that the terminal water in RNR−X binds with the Fe(III) center, which is also consistent with the earlier proposal based on analysis of ENDOR spectra.[14]

Before analyzing the hyperfine constants of the bridging oxygen species, we will first compare the ^{57}Fe hyperfine results. Although we present the three calculated principal values of the **A**-tensors of the Fe sites for all models, we will mainly focus on the anisotropic components. It is well known that the isotropic hyperfine coupling constants of metal centers theoretically are very difficult to predict quantitatively.[35,44] Here again, we see that the calculated ^{57}Fe isotropic hyperfine coupling constants are less than half of the observed ones for the current

(44) (a) Wilk, L.; Vosko, S. H. *Phys. Rev. A* **1977**, *15*, 1839−1846. (b) Neese, F. *J. Chem. Phys.* **2003**, *118*, 3939−3948.

Table 2. Calculated Fe Nuclear Densities ($\rho(0)$, shifted by $-11883.0\ a_0^{-3}$), Isomer Shifts (δ, mm s^{-1}), Quadrupole Splittings (ΔE_Q, mm s^{-1}), η Values, and Hyperfine Coupling Constants (MHz) for RNR−X Active Site Y122F Mutant-Type Models I, II, and III with Terminal H_2O in the Fe1(III)Fe2(IV)$\{S_1 = {}^5/_2,\ S_2 = -2\}$ State Compared with Experimental Results[a]

Mössbauer Properties

	Y122F							
	model I		model II		model III		experiments	
	Fe1	Fe2	Fe1	Fe2	Fe1	Fe2	*Fe(III)* [c]	*Fe(IV)* [c]
$\rho(0)$	0.678	1.547	0.916	1.424	1.385	1.437		
δ	0.56	0.22	0.47	0.27	0.28	0.26	*0.56(3)*	*0.26(4)*
ΔE_Q	0.55	−0.22	−0.40	−0.77	−0.76	−1.50	*−0.9(1)*	*−0.6(1)*
η	0.69	0.38	0.56	0.95	0.38	0.66	*0.5(2)*	*2.7(3)*

Proton Hyperfine Coupling Constants

	Y122F								
	model I		model II			model III		experiments	
	H_{t1} [b]	H_{t2} [b]	H_{t1}	H_{t2}	H_{br}	H_{t1}	H_{t2}	H_{t1} [d]	H_{t2} [d]
A_1	−10.93	−10.71	−9.64	−11.86	−15.28	−7.00	−10.75	*−10.25*	*−8.8*
A_2	−6.14	−6.34	−4.83	−6.33	3.26	−3.76	−5.80	*−10.25*	*−8.8*
A_3	18.99	17.33	20.88	17.46	19.58	24.34	17.43	*20.5*	*17.6*
A^{iso}	0.64	0.09	2.14	−0.24	2.52	4.53	0.29	*0.0*	*0.0*

^{17}O Hyperfine Coupling Constants

	Y122F									
	model I			model II			model III		experiments	
	O1	O2	O3	O1	O2	O3	O1	O3	O_{br} [e]	O_t [e]
A_1	8.57	12.48	−14.39	−1.85	−12.23	−16.18	−8.57	−13.69	*−0.0(10)*	*−17.0(5)*
A_2	−19.00	−19.72	−16.61	−7.07	−18.22	−21.42	−22.05	−21.76	*−22.5(5)*	*−20.5(5)*
A_3	−24.10	−26.80	−32.12	−29.24	−31.56	−35.68	−25.39	−27.32	*−23.5(5)*	*−34.0(5)*
A^{iso}	−11.51	−11.35	−21.04	−12.72	−20.67	−24.43	−18.67	−20.92	*−15.3*	*−23.8*
A_1^{aniso}	20.08	23.83	6.65	10.87	8.44	8.24	10.10	7.23	*15.3*	*6.8*
A_2^{aniso}	−7.49	−8.37	4.43	5.65	2.45	3.01	−3.38	−0.83	*−7.2*	3.3
A_3^{aniso}	−12.59	−15.46	−11.08	−16.52	−10.89	−11.25	−6.72	−6.40	*−8.2*	*−10.2*

^{57}Fe Hyperfine Coupling Constants

	Y122F							
	model I		model II		model III		experiments	
	Fe1	Fe2	Fe1	Fe2	Fe1	Fe2	Fe(III)[c]	Fe(IV)[c]
A_1	−34.35	1.06	−34.10	0.22	−26.27	−4.83	*−74.2(2)*	*27.5(2)*
A_2	−31.26	16.59	−24.09	24.00	−20.86	15.43	*−72.2(2)*	*36.8(2)*
A_3	−31.76	14.48	−26.32	14.70	−9.64	17.21	*−73.2(2)*	*36.8(2)*
A^{iso}	−32.45	10.71	−28.17	12.97	−18.93	9.42	*−73.2*	*33.7*
A_1^{aniso}	−1.89	−9.65	−5.93	−12.75	−7.35	−13.80	*−1.0*	*−6.2*
A_2^{aniso}	1.20	5.88	4.08	11.02	−1.93	6.01	*1.0*	*3.1*
A_3^{aniso}	0.70	3.77	1.85	1.73	9.28	7.79	*0.0*	*3.1*

[a] DFT-calculated **A**-tensors were rescaled by the spin coupling factors (see text). A^{iso} represents the isotropic **A**-tensor component, and A^{aniso} stands for the anisotropic **A**-tensor component. Values in parentheses correspond to standard experimental error. [b] H_{t1} is the proton on the terminal (t) water which H-bonds to Glu238, and H_{t2} is another proton H-bonding to Asp84. [c] From ref 4a. [d] From ref 14. [e] From ref 16. The relative signs of the three principal values were determined in the $^{17}O_2$ and $H_2{}^{17}O$ ENDOR experiments, but the absolute signs are not known. We have set the signs according to our calculations, respecting the relative signs set by experiment. We also reordered the **A**-tensor components for convenience so that $|A_3|$ is largest.

three models, similar to the scaling factors observed in other high-spin Fe and Mn systems.[35,44] Now comparing the calculated anisotropic ^{57}Fe hyperfine components, again, model I is the best and model III is the worst among these three models in reproducing the corresponding experimental results.

Now we examine the properties of the bridging oxygen species (O1 and O2 in the model clusters and the associated protons). It has been suggested from the $^{1,2}H$ and $^{17}O_2$ ENDOR experiments that there are two protons (in terminal water) and only one bridging oxygen (O_{br}) in the active site of RNR−X.[16] Within our current three models, only model III contains one bridging μ-oxo (O1). Its principal **A**-tensor value, A_1 (−8.57 MHz), deviates from the experimental value of -0 ± 1 MHz. However, its A_2 (−22.05 MHz) and A_3 (−25.39 MHz) are consistent with the observed values (−22.5 and −23.5 MHz). The bridging ^{17}O tensor result does not exclude model III; other experimental data are more definitive.

Our model II contains one bridging oxo and one bridging hydroxide. Though A_3 (22.57 MHz) of H_{br} (the proton on the bridging hydroxide) is close to one of the experimentally observed values, 20.5 MHz, the overall principal values and orientations of the **A**-tensor for H_{br} are very different from those for H_{t1}. If this proton exists, it should be observed by the $^{1,2}H$ ENDOR experiments.[14] The calculated **A**-tensors (including orientations) of O1 and O2 are very different. Though the principal eigenvalues for O2 and O3 are close to each other, their orientations are different. Therefore, if this model represents the active site of RNR−X, the $^{17}O_2$ and $H_2{}^{17}O$ ENDOR experiments should show three distinct signals.

Our model I contains two μ-oxo bridges (O1 and O2). We notice that the calculated **A**-tensor principal values of the two bridging oxo atoms are very close to each other, and similar to the corresponding ones of model III (except for the sign of A_1). For models I and III, A_2 and A_3 are in very good agree-

Table 3. Calculated Fe Nuclear Densities ($\rho(0)$, shifted by -11883.0 a_0^{-3}), Isomer Shifts (δ, mm s^{-1}), Quadrupole Splittings (ΔE_Q, mm s^{-1}), η Values, and Hyperfine Coupling Constants (MHz) for Native-Type RNR−X Active Site Models I, II, and III (Figures 4−7) with Terminal H_2O, $(H_2O)_t$, or Terminal OH^-, $(OH^-)_t$, and the Large Model X_{2nd} with Terminal H_2O (Figure 2 of Ref 21), in the Fe1(III)Fe2(IV)$\{S_1 = {}^5/_2, S_2 = -2\}$ State

Mössbauer Properties

	$(H_2O)_t$								$(OH^-)_t$					
	model I		model II		model III		model X_{2nd}[a]		model I		model II		model III	
	Fe1	Fe2	Fe1	Fe2	Fe1	Fe2	Fe1	Fe2	Fe1	Fe2	Fe1	Fe2	Fe1	Fe2
$\rho(0)$	0.662	1.546	0.888	1.430	0.899	1.411	0.552	1.073	0.931	1.439	1.294	1.205	1.402	1.161
δ	0.57	0.22	0.48	0.27	0.47	0.27	0.61	0.41	0.46	0.26	0.32	0.35	0.28	0.37
ΔE_Q	0.53	−0.23	−0.33	−0.71	0.74	−0.51	−1.50	0.95	−0.22	0.51	0.25	0.16	0.59	0.14
η	0.44	0.49	0.25	0.79	0.96	0.64	0.91	0.91	0.08	0.38	0.62	0.57	0.50	0.22

Proton Hyperfine Coupling Constants

	$(H_2O)_t$									$(OH^-)_t$			
	model I		model II			model III		model X_{2nd}[a]		model I	model II		model III
	H_{t1}	H_{t2}	H_{t1}	H_{t2}	H_{br}	H_{t1}	H_{t2}	H_{t1}	H_{t2}	H_{t1}	H_{t1}	H_{br}	H_{t1}
A_1	−10.14	−9.97	−8.82	−10.73	−17.90	−8.98	−11.99	−10.22	−8.24	−5.05	−4.54	14.13	−5.04
A_2	−5.67	−6.25	−4.20	−6.29	3.70	−7.25	−5.26	−6.49	−3.30	−1.08	1.02	1.88	−0.14
A_3	18.05	16.77	19.97	16.88	22.57	22.43	18.65	15.44	17.49	34.38	34.61	−15.67	35.99
A^{iso}	0.75	0.18	2.32	−0.05	2.39	2.07	0.46	−0.42	1.98	9.42	10.36	0.11	10.27

^{17}O Hyperfine Coupling Constants

	$(H_2O)_t$										$(OH^-)_t$							
	model I			model II			model III		model X_{2nd}[a]		model I			model II			model III	
	O1	O2	O3	O1	O2	O3	O1	O3	O1	O3	O1	O2	O3	O1	O2	O3	O1	O3
A_1	8.57	12.19	−15.68	−2.19	−11.97	−18.45	−9.45	−18.11	3.82	−15.58	13.57	13.35	−11.98	2.43	−11.97	−18.45	−3.60	−10.62
A_2	−19.64	−20.29	−17.87	−8.68	−18.28	−24.09	−20.41	−24.94	−0.99	−17.05	−22.17	−21.62	−25.15	−4.48	−18.28	−24.09	−13.05	−18.01
A_3	−23.58	−25.32	−32.91	−28.54	−30.88	−37.69	−31.50	−41.27	−21.22	−33.20	−27.94	−28.22	−34.99	−23.99	−30.88	−37.69	−27.55	−49.31
A^{iso}	−11.55	−11.14	−22.16	−13.14	−20.38	−26.74	−20.46	−28.11	−6.13	−21.94	−12.18	−12.16	−24.04	−8.68	−20.38	−26.74	−14.73	−25.98
A_1^{aniso}	20.12	23.33	6.47	10.95	8.41	8.29	11.00	10.00	9.95	6.36	25.75	25.51	12.06	11.11	8.41	8.29	11.14	15.36
A_2^{aniso}	−8.09	−9.15	4.28	4.45	2.10	2.66	0.04	3.16	5.14	4.89	−10.00	−9.45	−1.11	4.20	2.10	2.66	1.68	7.97
A_3^{aniso}	−12.03	−14.18	−10.76	−15.40	−10.51	−10.95	−11.04	−13.16	−15.09	−11.26	−15.76	−16.06	−−10.95	−15.31	−10.51	−10.95	−12.82	−23.33

^{57}Fe Hyperfine Coupling Constants

	$(H_2O)_t$								$(OH^-)_t$					
	model I		model II		model III		model X_{2nd}[a]		model I		model II		model III	
	Fe1	Fe2	Fe1	Fe2	Fe1	Fe2	Fe1	Fe2	Fe1	Fe2	Fe1	Fe2	Fe1	Fe2
A_1	−34.47	1.72	−34.60	0.36	−30.07	0.74	−33.20	7.38	−27.96	−3.05	−20.36	−7.32	−18.95	1.10
A_2	−30.99	16.86	−24.57	23.48	−22.68	22.10	−18.39	14.32	−23.55	16.54	−15.03	18.71	−17.36	7.10
A_3	−31.74	14.92	−26.09	15.13	−25.19	11.93	−24.91	24.20	−24.61	15.27	−4.96	21.62	−6.66	26.57
A^{iso}	−32.40	11.17	−28.42	12.99	−25.98	11.59	−25.50	15.30	−25.37	9.58	−13.45	11.01	−14.32	11.59
A_1^{aniso}	−2.07	−9.45	−6.18	−12.63	−4.09	−10.85	−7.70	−7.92	−2.59	−12.64	−6.91	−18.32	−4.62	−10.49
A_2^{aniso}	1.41	5.69	3.85	2.14	3.31	10.51	7.11	−0.98	1.82	6.95	−1.58	7.71	−3.04	−4.49
A_3^{aniso}	0.66	3.76	2.33	10.49	0.79	0.34	0.59	8.90	0.76	5.68	8.49	10.62	7.66	14.98

[a] The core structure of X_{2nd} was shown in Figure 3 of the present paper. Other properties of this cluster was given in Table 1 of ref 21.

ment with the experiment, but A_1 has a larger deviation. In addition to the values, the principal axes of the two **A**-tensors of O1 and O2 in model I are also in very similar directions. The calculated eigenvectors $A_i(x,y,z)$ of O1 in model I are $A_1(-0.269,-0.953,-0.139)$, $A_2(0.861,-0.302,0.410)$, and $A_3(-0.433,-0.010,0.902)$. The corresponding ones for O2 are $A_1(-0.219,-0.961,0.167)$, $A_2(0.913,-0.142,0.381)$, and $A_3(-0.343,0.236,0.909)$, respectively. The coordinates of the geometries have been arranged as Fe1 at the (0,0,0) center, Fe2 on the *x*-axis, and the vector product (Fe1−O1)×(Fe1−O2) in the *x*−*y* plane. The very similar **A**-tensors of O1 and O2 may explain why only one O_{br} signal has been observed from the $^{17}O_2$ ENDOR experiments. Since model I is the best in reproducing the Fe−Fe distance from analysis of EXAFS experiments, Mössbauer isomer shift and quadrupole splitting data, and the ^1H and ^{17}O hyperfine coupling constants of the terminal water for RNR−X, we therefore propose that the class I RNR intermediate X has two μ-oxo bridges, which are derived from an O_2 molecule and do not exchange with the solvent, since the $H_2{}^{17}O$ ENDOR experiment shows only signals for the terminal oxygen.[16] The terminal water would therefore originate from the solvent and would not be observed in the $^{17}O_2$ ENDOR experiment (see Figure 7). Burdi et al.[16] have found that, starting from $^{17}O_2$, a bridging (O_b) and terminal-type (O_t) signal are seen in the CW ENDOR spectra of ^{17}O quenched at 42 ms. Since this terminal-type signal disappears when the reaction is freeze-quenched at 4030 ms, they interpret this as formation of terminal bound $H_2{}^{17}O$, which then exchanges with bulk solvent. In contrast, we interpret the disappearance of the $^{17}O_t$ signal differently. In our model (Figure 7), an unstable terminal ^{17}OH is bound to Fe1(III) along with the bridging ^{17}O starting from $^{17}O_2$ in an early intermediate that precedes intermediate X, called Pre-X(t). As this terminal ^{17}OH goes bridging (Pre-X(b)) and deprotonates, the $^{17}O_t$ signal is lost. In the $H_2{}^{17}O$ "wash-in" CW ENDOR experiment, starting from labeled $H_2{}^{17}O$ and unlabeled O_2, a terminal ^{17}O signal is seen at different experimental times. This signal is more intense (factor about 2) when the sample is quenched at 4030 ms than at 42 ms. Burdi et al. interpret this as $H_2{}^{17}O$ exchanging with the Fe(III)-bound water formed from O_2. We interpret this as $H_2{}^{17}O$ binding to a separate site, and at

early times (around 42 ms) the $H_2{}^{17}O$ involved in binding may be more disordered, so that the ENDOR signal is less intense.

In addition, the calculated pK_a value (4.02, see Table 1) for the process of {model II−Y122F$(OH^-)_{br}$ → model I−Y122F-$(O^{2-})_{br} + H^+$} shows that the preferred protonation state is the di-μ-oxo form (model I over model II). The broken-symmetry state and spin-projected energies (Table S3) also support that model I in the Fe1(III)Fe2(IV)$\{S_1 = {}^5/_2, S_2 = -2\}$ state is more stable than its Fe1(IV)Fe2(III)$\{S_1 = -2, S_2 = {}^5/_2\}$ state. Overall, by comparing all the properties mentioned above, we propose that the Fe1(III)Fe2(IV)$\{S_1 = {}^5/_2, S_2 = -2\}$ state of our model I (Figure 4) with a terminal water represents the active site structure of the class I RNR intermediate state X.

To make this argument stronger, we compare next the properties of the Y122F models with the native forms and see if these conclusions still hold for the native clusters. Since the ^{1,2}H ENDOR experiments did not exclude the possibility of a terminal hydroxide in RNR−X, we will also examine the pK_a values for the terminal water molecule and see how the properties change if the three models have a terminal hydroxide rather than a water molecule. The geometrical structures of these three models with a terminal hydroxide are similar to those of Figures 4, 5, and 6 by deleting the proton on O3 which H-bonds with $O_{\delta 2}$ of Asp84. All calculated Mössbauer and Hyperfine properties of the native-type models in the Fe1(III)Fe2(IV)$\{S_1 = {}^5/_2, S_2 = -2\}$ state with either terminal water or terminal hydroxide are given in Table 3.

3.2. Native-Type Models I, II, and III with Terminal H_2O or Terminal Hydroxide in the Fe1(III)Fe2(IV) State. The calculated properties, including the geometries (Table 1), net spin population of the Fe sites, isomer shifts, quadrupole splittings, and all ^{1}H, ^{17}O, and ^{57}Fe hyperfine coupling constants (Tables 2 and 3), are almost the same for model I−$(H_2O)_t$ in the Y122F and native forms. As mentioned before, most of the experiments for RNR−X were performed and reported mainly for the mutant Y122F−R2 proteins. It is, therefore, very important that the measurements do reflect the properties of the native-type proteins. Our calculations for model I indeed support the assumption that the native and Y122F-form RNR−X have similar geometric and spectroscopic properties. The calculated pK_a value (2.51, see Table 1) for the process of {model II−native$(OH^-)_{br}$ → model I−native$(O^{2-})_{br} + H^+$} shows that model I is still preferred over model II in the native-type models. All corresponding properties of model II−$(H_2O)_t$ in the Y122F and native forms are also similar to each other. For model III, there exist large discrepancies between the native and mutant forms on the calculated properties of Fe1−O1 distance (Table 1), isomer shift of Fe1, quadrupole splittings of both Fe sites, and all ^{17}O and ^{57}Fe hyperfine coupling constants. Therefore, the properties of the mutant form model III cannot represent the corresponding properties of its wild-type (wt) partner. These differences between model III Y122F mutant versus native contradict the observation, reported by Burdi et al.,[16] that ^{57}Fe ENDOR measurements "disclose no structural differences between X(wt) and X(Y122F)". The conclusion of section 3.1 still holds. That is, most of the calculated properties of the geometries, Mössbauer, and hyperfine coupling constants for Fe1(III)Fe2(IV)$\{S_1 = {}^5/_2, S_2 = -2\}$ state model I (both native and Y122F forms) with a terminal water are consistent with the experiments.

The pK_a values (Table 1) for the terminal water in the process of $\{(H_2O)_t \rightarrow (OH^-)_t + H^+\}$ show that the terminal water form is highly preferred in model I (pK_a = 13.20). The pK_a values are 7.38 and 7.60 for models II and III, respectively, showing that the terminal water and hydroxide forms may coexist in models II and III. The calculated isomer shifts, and especially the ^1H_t hyperfine coupling constants for the $(OH^-)_t$ models are much worse than the corresponding $(H_2O)_t$ ones. We therefore exclude the possibility that there is a terminal hydroxide instead of a terminal water in the class I RNR−X active site.

3.3. Model X_{2nd}{Fe1(III)Fe2(IV)−$(H_2O)_t$}. As mentioned in the Introduction, our X_{2nd}{Fe1(III)Fe2(IV)−$(H_2O)_t$} model (ref 21, our second study on possible models of RNR−X) was constructed closely following the structure for RNR−X proposed by Burdi et al.[16] The cluster was shown in Figure 2 of ref 21, and its core structure is given in Figure 3 of the present paper. The geometrical properties obtained from geometry optimization were given in Table 1 of ref 21. From energetic and pK_a analysis, this cluster is not likely to represent the active site of RNR−X. We therefore did not perform the Mössbauer and hyperfine calculations for this cluster in ref 21. Now, to complete this study and to compare this model with our current Fe1(III)Fe2(IV) state model I−$(H_2O)_t$ results, we have performed the Mössbauer and hyperfine calculations for this model and also presented the results in Table 3. Since it is a very large model, including the second-shell H-bonding partners, the calculations were performed only in the gas phase.

Compared with the experimental data, the calculated isomer shifts, the ^{1}H hyperfine **A**-tensors, and the anisotropic components of the ^{57}Fe hyperfine coupling constants of this X_{2nd}{Fe1-(III)Fe2(IV)−$(H_2O)_t$} model are worse than the corresponding results for both the native and Y122F Fe1(III)Fe2(IV) state model I−$(H_2O)_t$ clusters (Tables 1 and 2). There is only one bridging oxygen (O1) in the X_{2nd}{Fe1(III)Fe2(IV)−$(H_2O)_t$} model. However, the calculated hyperfine coupling constants of this bridging oxygen are not in agreement with the observed values. Experimentally, A_1 of O_{br} is close to zero, and A_2 and A_3 are large values with the same sign. The calculated A_1 and A_2 of O1 are all very small (close to zero), resulting in a too-small isotropic value and different ordering of the anisotropic components compared with the observed ones. Therefore, the Mössbauer and hyperfine calculations also support our previous conclusion that the X_{2nd}{Fe1(III)Fe2(IV)−$(H_2O)_t$} model, though constructed closely following the experimentally proposed structure for RNR−X, is not likely to represent the active site of RNR−X.

3.4. Estimates of the Fe(IV) d−d Transition Energies for the Above Models in the Fe1(III)Fe2(IV)−$(H_2O)_t$ State. The RFQ-MCD absorption spectra on the double mutant Y122F/Y356F−X have been reported for the first time.[9a] Three low-energy bands at 16 700, 19 400, and 22 100 cm^{-1} (or 2.07, 2.41, and 2.74 eV) were assigned as the lowest spin-allowed ligand field d−d transitions of an Fe(IV) site. The authors then calculated the d-orbital energy levels and wave functions from a ligand field model for mono-μ-oxo- and bis-μ-oxo-bridged dimers using crystallographically characterized octahedral Mn model complexes.[9a] They found that the calculated Fe(IV) d−d transition energies (11 500, 19 800, and 26 300 cm^{-1}, or 1.43, 2.46, and 3.26 eV) for a mono-μ-oxo-bridged structure were low relative to those for the bis-μ-oxo structure (14 900, 25 300,

Table 4. Estimation of the Fe(IV) d−d Transitions for the Fe1(III)Fe2(IV)−$(H_2O)_t$-Type RNR−X Active Site Models

model	β orbital position[a]	Fe2(IV) d populations (%)	ϵ [b]	$\Delta\epsilon$[c] $\epsilon_{v1}-\epsilon_{occ}$	$\epsilon_{v2}-\epsilon_{occ}$	$\epsilon_{v3}-\epsilon_{occ}$
I−Y122F	n_H-10	z^2(7.8), xy(1.8), x^2-y^2(1.1)	−6.421	3.074		
	n_H-9	z^2(9.6), x^2-y^2(6.9)	−6.385	3.038		
	n_H-7	yz(5.0), z^2(1.6), xy(1.4)	−6.222	2.875		
	n_H-6	yz(8.7), xy(5.7), x^2-y^2(1.6)	−6.116	2.769		
	n_H-3	yz(5.3), xy(4.7), x^2-y^2(2.4)	−5.945	2.598		
	n_H	x^2-y^2(17.2), z^2(8.3), xy(7.5)	−5.110	1.763		
	$n_L+3=v1$	xz(41.2), yz(2.1)	−3.347			
II−Y122F	n_H-13	yz(6.5), z^2(1.2)	−7.245	3.177		
	n_H-11	yz(6.0), xy(1.2)	−7.049	2.981		
	n_H-10	xy(7.2), z^2(1.0)	−6.988	2.920		
	n_H-9	yz(4.3), xy(2.2), z^2(1.2)	−6.817	2.749		
	n_H-8	z^2(11.3), x^2-y^2(5.3), yz(2.8)	−6.743	2.675		
	n_H	x^2-y^2(15.8), z^2(9.3), xy(6.2)	−5.559	1.491		
	$n_L+3=v1$	xz(33.6), x^2-y^2(3.2), yz(1.5)	−4.068			
III−Y122F	n_H-10	z^2(12.4), xy(2.9), xz(1.9)	−7.358	2.087	2.636	3.227
	n_H-9	x^2-y^2(5.8), z^2(4.3), xz(4.2)	−7.176	1.905	2.454	3.045
	n_H-8	xy(15.5), x^2-y^2(2.3), yz(2.2)	−7.152	1.881	2.430	3.021
	n_H-7	xy(12.8), z^2(3.7), x^2-y^2(2.9), yz(2.5), xz(1.7)	−6.922	1.651	2.200	2.791
	n_H-6	xy(3.2), yz(3.1), xz(2.5)	−6.780	1.509	2.058	2.658
	n_H-5	x^2-y^2(5.4), z^2(2.7), yz(1.4)	−6.590	1.319	1.868	2.459
	n_H-3	yz(21.6), xy(11.3), x^2-y^2(4.3)	−6.211	0.940	1.489	2.080
	$n_L+1=v1$	xz(6.3), yz(3.4), xy(1.5)	−5.271			
	$n_L+3=v2$	x^2-y^2(6.6), yz(5.7), xz(5.0), z^2(3.1)	−4.722			
	$n_L+4=v3$	xz(5.3), x^2-y^2(5.0), yz(1.7), z^2(1.6)	−4.131			
X_{2nd}	n_H-30	xz(9.4), z^2(6.8), yz(4.2), x^2-y^2(1.4)	−7.794	2.795	3.685	
	n_H-27	z^2(11.2), x^2-y^2(2.6)	−7.544	2.545	3.435	
	n_H-20	z^2(12.0), x^2-y^2(2.6), xy(1.1)	−6.959	1.960	2.850	
	n_H-14	xz(6.0), xy(5.6), x^2-y^2(5.3), yz(2.7)	−6.555	1.556	2.446	
	n_H-4	xy(9.3), z^2(4.0), x^2-y^2(2.2), xz(1.7)	−5.557	0.558	1.448	
	n_H-3	xy(6.9), z^2(2.7), x^2-y^2(1.7), xz(1.4)	−5.500	0.501	1.391	
	n_H-2	yz(7.4), xz(3.5)	−5.011	0.012	0.902	
	$n_L=v1$	yz(5.7), xz(2.6)	−4.999			
	$n_L+3=v2$	yz(9.6), xz(4.4), xy(2.0)	−4.109			

[a] n_H and n_L represent the positions of the β spin (the majority spin on the Fe(IV) site) HOMO and LUMO, respectively. [b] Molecular orbital energy in eV. [c] The energy difference (eV) between the occupied (occ) and virtual (v) orbitals gives the estimation of the transition energy. The experimentally observed first spin-allowed Fe(IV) d−d transition energies in MCD for Y122F/Y356F−X are at 2.07, 2.41, and 2.74 eV.[9a]

and 29 100 cm^{-1}, or 1.85, 3.14, and 3.61 eV), and the former were closer to the experimental data. Their analysis therefore favored the mono-μ-oxo model for X.

To estimate the Fe(IV) d−d transition energies of our models, in Table 4 we compare the molecular orbital energy differences between the occupied and virtual orbitals which contain significant Fe(IV)-d populations. The compared models I, II, and III are in Y122F form. Only model I adopts the bis-μ-oxo structure. Models II, III, and X_{2nd} all have a mono-μ-oxo structure.

The lowest transition energies in model I−Y122F are in good agreement with the observed bands. On the basis of orbital energies and character, we can reasonably assign band 1, $n_H \rightarrow n_L + 3$ (1.763 eV); band 2, $n_H - 3$, $n_H - 6 \rightarrow n_L+3$ (2.598 − 2.769 eV); and band 3, $n_H - 7$, $n_H - 9$, $n_H - 10 \rightarrow n_L + 3$ (2.875 − 3.074 eV). The Fe2(IV) d−d transitions are relatively easier to analyze for our models I and II, since only one virtual orbital ($n_L + 3$, see Table 4) in the two models contains significant Fe2(IV)-d populations, and the total contribution of the Fe2(IV)-d orbitals to the virtual molecular orbital is as high as 43%. On the other hand, the Fe2(IV)-d characters are distributed in two or three virtual orbitals in model III and X_{2nd}, with much smaller percentages of Fe(IV)-3d populations in each virtual orbital. Therefore, the d−d transitions in model III and X_{2nd} are probably mixed between different occupied and virtual orbitals. The first band of the Fe(IV) d−d transition energies in models II, III, and X_{2nd} are too low, and the overall low-lying d−d transition energies, particularly for models III and X_{2nd}, are poorer than for model I compared with the MCD observed bands (2.07, 2.41, and 2.74 eV). In addition, we expect that electron relaxation effects should prove small for these Fe(IV) d−d transition energies. More complex and accurate calculations of Fe(IV) d−d excited states are in progress.

4. Conclusions

In this paper, three kinds of active site models (Figures 4−6) for class I RNR intermediate X have been studied using broken-symmetry density functional theory incorporated with the COSMO solvation model. Other kinds of models have also been investigated in our former studies of proposed RNR−X-type species.[19−21] By comparing the calculated properties, including geometries, energies, pK_a values, spin states, ^{57}Fe, ^{1}H, and ^{17}O hyperfine tensors, Mössbauer isomer shift and quadrupole splitting constants, and the Fe(IV) d−d transition energies, among the different models and with the available experimental data, we find that our current model I (Figure 4), which contains two μ-oxo bridges and a terminal water in the Fe1(III)Fe2(IV)-$\{S_1 = {}^5/_2, S_2 = -2\}$ spin state, represents the active site structure of class I RNR intermediate X well.

It is well known that the active site of methane monooxygenase (MMOH) is very similar to that of RNR−R2.[45] The

(45) Valentine, A. M.; Tavares, P.; Pereira, A. S.; Davydov, R.; Krebs, C.; Hoffman, B. M.; Edmondson, D. E.; Huynh, B. H.; Lippard, S. J. *J. Am. Chem. Soc.* **1998**, *120*, 2190−2191.

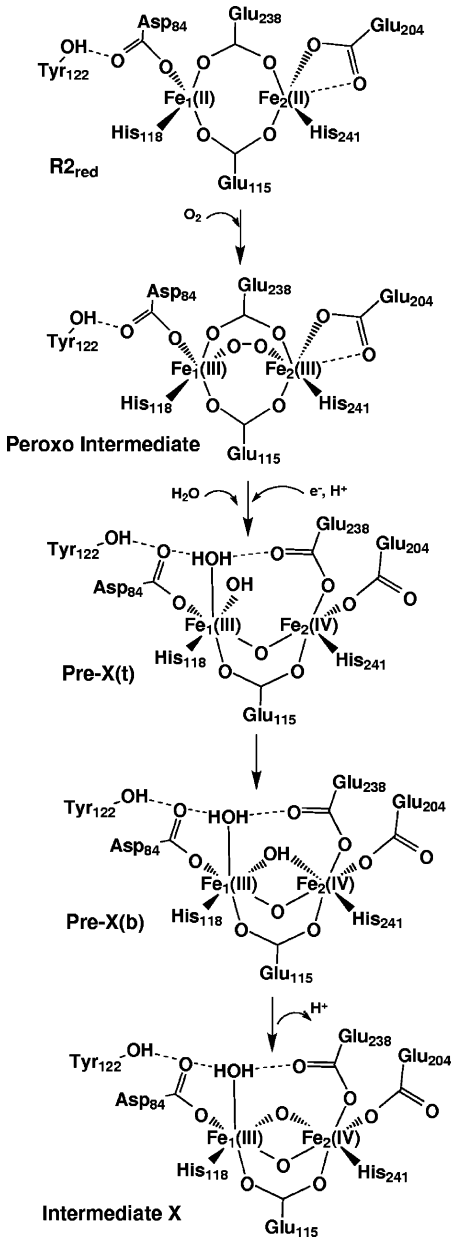

Figure 7. Feasible path showing how RNR−X is formed by the reaction of O_2 with the reduced RNR−R2 diiron center.

intermediate Q of MMOH has been proposed, and substantial spectroscopic evidence and DFT models favor an Fe(IV)Fe(IV) center with di-μ-oxo bridges.[34a,46] The radiolytically reduced Q (Q_x) then likely contains an Fe(III)Fe(IV) center with either di-μ-oxo or one μ-oxo and one bridging hydroxide. The fact that Q_x and X have similar Mössbauer parameters (Table 1 in ref 45) supports the proposition of similar geometrical structures for Q_x and X. Further spectroscopic data on Q_x would be extremely valuable to test this proposal.

We also propose that the two bridging oxygens of RNR−X originate from the O_2 molecule, and that the terminal water comes from the solvent. Figure 7 briefly shows how we propose RNR−X is formed by the reaction of O_2 with the reduced RNR−R2 diiron center.

According to both experimental and theoretical studies, the diferric peroxo intermediate of RNR likely has a *cis*-μ-1,2-peroxo coordination geometry.[9b] From the peroxo intermediate to X, an electron is transferred to the diiron center. Spectroscopic studies indicate that this electron is transferred from Trp48,[10c−e] which is near the surface of the protein and within the H-bonding network of Trp48···Asp237···His118. During the O−O cleavage, the carboxylate group of Glu238 has to tilt up, leaving an open space for one of the oxygen atoms moving to the other side. Meanwhile, a water molecule fills the vacant ligand site of Fe1 and H-bonds to both Glu238 and Asp84. This seems not in agreement with the interpretation of the ^{17}O and $H_2{}^{17}O$ ENDOR experiments,[16] where it was proposed that, starting from ^{17}O-labeled O_2, one oxygen becomes a bridge while the other becomes the terminal O of H_2O and then washes out. But the implications of the ENDOR time course are not so clear. We would propose instead that from the diferric peroxo complex one oxygen goes bridging, and the other O becomes first a terminal and subsequently a bridging OH^- in an unstable Fe(III)−O−Fe(IV) complex preceding RNR−X. Later this hydroxide deprotonates, forming finally a di-oxo bridge. This is energetically reasonable and fits the ENDOR spectroscopy and time course. The $H_2{}^{17}O$ "wash-in" ENDOR gives a terminal bound $H_2{}^{17}O$−Fe(III) at a different site, where this ^{17}O cannot go bridging, also consistent with ENDOR. Additional theoretical (computational) work is planned on the pathway between the peroxo intermediate and the intermediate X, and on how the active RNR with the Tyr122 radical is formed from the intermediate state X.

Acknowledgment. We thank NIH for financial support (GM43278 to L.N.). The generous support of computer resources of the Scripps Research Institute is gratefully acknowledged. W.H. also appreciates the support by NSF cooperative agreement ACI-9619020 through computing resources provided by the National Partnership for Advanced Computational Infrastructure at the San Diego Supercomputer Center. We thank Laura Hunsicker-Wang, Martin Bollinger, Edward Solomon, and Brian Hoffman for valuable discussions on spectroscopy.

Supporting Information Available: Iron complexes used in linear fitting of the isomer shift parameters, the comparison of the calculated and observed quadrupole splittings for 24 Fe complexes, the calculated results for the Fe1(IV)Fe2(III)$\{S_1 = -2, S_2 = {}^5/_2\}$ state models I and II, and the Cartesian coordinates of our COSMO-optimized geometries of the Fe1(III)Fe2(IV) state native and Y122F-form model clusters. The structural models X_{2nd}, I, II, and III with terminal water in Y122F form with superimposed coordinate systems are also given for comparison with Table 4. This material is available free of charge via the Internet at http://pubs.acs.org.

JA050904Q

(46) Baik, M.-H.; Newcomb, M.; Friesner, R. A.; Lippard, S. J. *Chem. Rev.* **2003**, *103*, 2385−2419.